



This open access document is posted as a preprint in the Beilstein Archives at <https://doi.org/10.3762/bxiv.2023.29.v1> and is considered to be an early communication for feedback before peer review. Before citing this document, please check if a final, peer-reviewed version has been published.

This document is not formatted, has not undergone copyediting or typesetting, and may contain errors, unsubstantiated scientific claims or preliminary data.

Preprint Title Deep-Red Fluorophore Based on Naphthothiadiazole as Emitter with HLCT, AIE and Ambipolar Transporting Properties for Electroluminescent Device

Authors Suangsiri Arunlimsawat, Patteera Funchien, Pongsakorn Chasing, Atthapon Saenubol, Taweesak Sudyoatsuk and Vinich Promarak

Publication Date 11 Juli 2023

Article Type Full Research Paper

Supporting Information File 1 Supporting information.docx; 805.0 KB

ORCID® iDs Taweesak Sudyoatsuk - <https://orcid.org/0000-0002-9160-1578>;
Vinich Promarak - <https://orcid.org/0000-0003-4805-9944>



License and Terms: This document is copyright 2023 the Author(s); licensee Beilstein-Institut.

This is an open access work under the terms of the Creative Commons Attribution License (<https://creativecommons.org/licenses/by/4.0>). Please note that the reuse, redistribution and reproduction in particular requires that the author(s) and source are credited and that individual graphics may be subject to special legal provisions.

The license is subject to the Beilstein Archives terms and conditions: <https://www.beilstein-archives.org/xiv/terms>.

The definitive version of this work can be found at <https://doi.org/10.3762/bxiv.2023.29.v1>

Deep-Red Fluorophore Based on Naphthothiadiazole as Emitter with HLCT, AIE and Ambipolar Transporting Properties for Electroluminescent Device

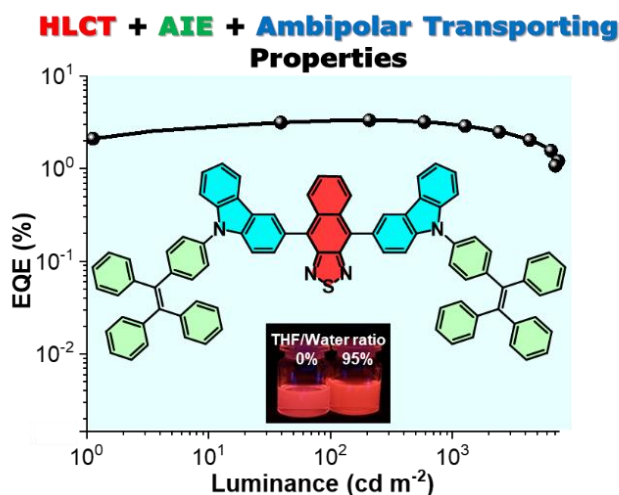
Suang Siri Arunlimsawat,¹ Patteera Funchien,¹ Pongsakorn Chasing,¹ Atthapon Saenubol,¹
Taweesak Sudyoasuk² and Vinich Promarak*¹

¹Department of Materials Science and Engineering, School of Molecular Science and Engineering, Vidyasirimedhi Institute of Science and Technology, Wangchan, Rayong 21210 Thailand

Email: vinich.p@vistec.ac.th

²Frontier Research Center, Vidyasirimedhi Institute of Science and Technology, Wangchan, Rayong 21210 Thailand

Abstract



Herein, we report the synthesis and characterization of an efficient ambipolar charge-carrier-transporting deep-red fluorophore (**TPECNz**) based on donor-acceptor-donor (D-A-D) type molecule and its application as a non-doped emitter in an organic light-emitting diode (OLED). **TPECNz** contains naphtho[2,3-c][1,2,5]thiadiazole (Nz) as a strong acceptor unit symmetrically functionalized with N-(4-(1,2,2-triphenylvinyl)phenyl)-carbazole as a donor and aggregation-induced emission (AIE) luminogen. The experimental (solvatochromic and emission in THF-water mixture studies) and theoretical investigations prove that **TPECNz** retains cooperative hybridized local and charge transfer (HLCT) and AIE features. Thanks to its D-A-D type structure with a proper twist angle between D and A units, a strong electron deficiency of Nz unit, and electron donating and hole-transporting natures of carbazole, **TPECNz** exhibits a strong deep red emission ($\lambda_{em} = 648$ nm) with a high fluorescence quantum yield of 96%, outstanding thermal property ($T_g = 236$ °C), and ambipolar charge-carrier-transporting property with a decent balance

of mobility of electron ($1.50 \times 10^{-5} \text{ cm}^2 \text{ V}^{-1} \text{ s}^{-1}$) and hole ($4.42 \times 10^{-6} \text{ cm}^2 \text{ V}^{-1} \text{ s}^{-1}$). **TPECNz** is successfully employed as a non-doped emitter in OLED which displays deep red electroluminescent emission peaked at 659 nm with CIE coordinates of (0.664, 0.335), an EQE_{max} of 3.32% and exciton utilization efficiency (EUE) of 47%.

Keywords

Deep-red fluorophore; Naphthothiadiazole; Ambipolar material; Aggregation-induced emission; Hybridized local and charge transfer; Organic light-emitting diode

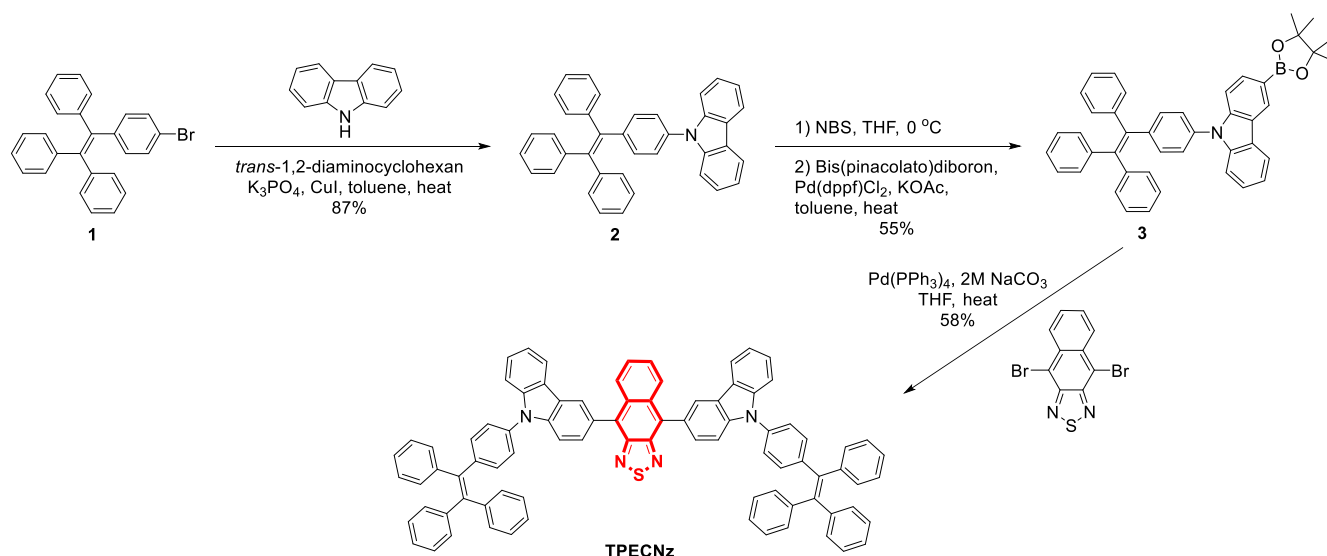
Introduction

Recently, organic fluorophores with efficient deep-red/near-infrared (DR/NIR) emission properties ($\lambda_{\text{em}} = 650\text{--}900 \text{ nm}$) have received much attention due to their potential applications in several different fields such as chemosensing,[1–3] bioimaging/biosensing,[4–8] photodynamic therapy,[9] optical communication,[10] NLO materials,[11] laser dyes,[12] and DR/NIR electroluminescent devices.[13–18] However, DR/NIR chromophores typically suffer from low photoluminescent quantum yields (Φ_{PL}) because of their intrinsic small band-gap energy causing larger vibronic coupling between the ground and excited states, particularly when they are applied as emitters in organic light-emitting diodes (OLEDs).[19] Therefore, with such a constrained number of efficient emitters, the current advance of DR/NIR OLEDs largely trails behind the visible light emission OLEDs.[20,21] So far, remarkable efforts have been made in designing new DR/NIR organic fluorophores in combination with device engineering to build up the performance of DR/NIR OLEDs. In general, to realize high fluorescence in the DR/NIR region from the organic fluorophores, the challenges of their pronounced non-radiative process, and high planarity and extended π -conjugation length which eventually favor the undesired formation of poorly emissive molecular aggregates must be overcome. Alternatively, donor-acceptor (D-A) type organic fluorophores have been introduced and successfully exploited for the development of fluorophores with DR/NIR emissions without lengthy extension of their π -conjugation systems due to a broadening of both the valence and the conduction bands and a consequent narrowing of the energy gap.[22–25] The D-A characters also offer a tunability of optoelectronic properties such as energy levels, optical bandgap (E_{g}), and charge transport properties, which could be done by selecting different D and A moieties.[22,26–28] In these fluorophores, the emission generally derives from intramolecular charge transfer (CT) states at lower energy. Nonetheless, the formed CT state between D and A in such materials normally caused lesser Φ_{PL} because of the separated frontier molecular orbitals.[29,30] Recently, the reports by Ma et al. revealed that by designing

suitable twist-angles between D and A, and D-A strength, frontier molecular orbitals of D-A fluorophore are not completely separated due to overlap between the transition orbitals.[31–33] In these molecules, the lowest excited-state still shows moderate or large oscillator strengths or a mixing of two excited state components, locally excited (LE) state and CT excited state. This kind of excited state was later known as a hybridized local and charge transfer (HLCT) state, in which the CT component can provide a high-lying reversed intersystem crossing (hRISC) pathway for fast and effective triplet utilization in the device, and the LE component can contribute good Φ_{PL} . [34–36] So far, based on this concept, several D-A-type fluorophores have been designed and investigated including some DR/NIR materials.[37–41] Inevitably, these materials displayed high Φ_{PL} and exceptional OLED device performance.[42–45] Even though the radiative transition rate is improved for the HLCT fluorophores, the non-radiative transition process is still an obstacle to lowering the Φ_{PL} , particularly for the DR/NIR emitters.[20,46] Therefore, to enhance the performance of HLCT-based DR/NIR fluorophores the non-radiative transition process of the excited state needs to be resolved. This could be managed by the molecular design of D-A structure. It has been reported that the performance of HLCT fluorophores greatly depends on the ability of donors, acceptors, and π spacers and the building blocks of HLCT should be carefully selected to regulate appropriate electron push–pull strength.[32,35,47,48]

Here, a novel D-A chromophore, 4,9-bis(9-(4-(1,2,2-triphenylvinyl)phenyl)-9H-carbazol-3-yl)naphtho[2,3-c][1,2,5]thiadiazole (**TPECNz**), built on the D-A-D type structure was designed and synthesized (Scheme 1). The D-A-D configuration was constructed by incorporating a second symmetrical donor in the D-A framework, which could further reduce the energy gap between HOMO/LUMO hybrid orbits and drive fluorescence emission to longer wavelengths.[48,49] In this molecular design, the strong electron deficiency naphtho[2,3-c][1,2,5]thiadiazole (Nz)[13,50,51] as an acceptor and strong electron donating carbazole[52] as a donor unit were used in the D-A-D structure to further reduces the bandgap, thereby red-shifting the absorption and emission wavelengths. In addition, the strong electron affinity of Nz and the electron-donating and hole-transporting ability of carbazole would build in the good ability to transport electrons and holes, respectively, providing well-balanced ambipolar characteristics. While the attached 4-(1,2,2-triphenylvinyl)phenyl (TPE) moiety would induce the aggregation-induced emission (AIE) feature to the molecule. It was suspected that AIE would restrain the aggregation-caused quench (ACQ) and the energy loss through the vibronic coupling natures of the DR/NIR fluorophores.[53] As a result, **TPECNz** effectively possessed a strong deep red emission with combined HLCT, AIE, and ambipolar transporting properties, which enable its application as a non-doped emitter.

The **TPECNz**-based non-doped deep red OLED realized a maximum external quantum efficiency (EQE_{max}) of 3.32% with an emission peak at 659 nm.



Scheme 1: Synthesis of **TPECNz**.

Results and Discussion

The designed **TPECNz** molecule was synthesized by a multi-step reaction as described in Scheme 1. Initially, an Ullmann coupling reaction of bromo-TPE **1** and carbazole provided a TPE-N-carbazole **2** in good yield. The resultant was converted to the boronic ester intermediate **3** in 55% yield in two steps: mono-bromination at the carbazole unit of **2** with NBS/THF at low temperature giving the unisolated mixed brominated product followed by borylation with bis(pinacolato)diboron catalyzed by Pd(dppf)Cl₂/KOAc. Finally, **TPECNz** was attained as red solids in a reasonable yield by a Suzuki-type cross-coupling reaction between **3** and 4,9-dibromonaphtho[2,3-c][1,2,5]thiadiazole. Its chemical structure and purity were verified by ¹H-NMR, ¹³C-NMR, and high-resolution MALDI-TOF-MS techniques.

To examine the electronic properties of D–A **TPECNz**, density functional theory (DFT) calculations at the B3LYP level with 6-31G (d,p) basis set were performed. It has been previously reported that the twist angle of the D–A segment had a significant role in controlling the CT component in the HLCT state.[54] A suitable twisted angle (40–80°) allocated an appropriate tuning between the complete π - conjugation and the pure CT transition character to form the HLCT state. As depicted in Figure 1a, the optimized structure of **TPECNz** revealed a twisting molecular configuration with dihedral angles between the planes of terminal carbazole donors and Nz acceptor of 54–56° which will benefit the state mixing between the LE and CT states. The lowest unoccupied molecular orbital (LUMO) was mainly localized on the Nz ring, while the highest occupied molecular orbital (HOMO) was delocalized over the Nz core and attached

carbazole moieties. There was an overlap between the HOMO and LUMO orbitals over the Nz fragment, which is likely to promote the LE component and consequently gives rise to a faster radiative decay and thus a higher luminescence efficiency. To further figure out its excited-state properties, the natural transition orbitals (NTOs) of singlet (S) and triplet (T) excited states were executed based on time-dependent (TD)-DFT calculations at the CAM-B3LYP/6-31G(d) level of theory. As shown in Figure 1b, the hole and particle of **TPECNz** are similar to its HOMO and LUMO orbitals, respectively. The $S_0 \rightarrow S_1$ transition with oscillator strength (f) of 0.476 clearly showed the HLCT transition characteristics, in which a certain overlap between hole and particle wavefunctions on the Nz ring represented for LE component inducing a high luminescence efficiency, while a significant spatial separation between hole and particle wavefunctions considered for CT component promoting RISC process along high-lying excitation state for enhancing an exciton utilization efficiency (EUE).

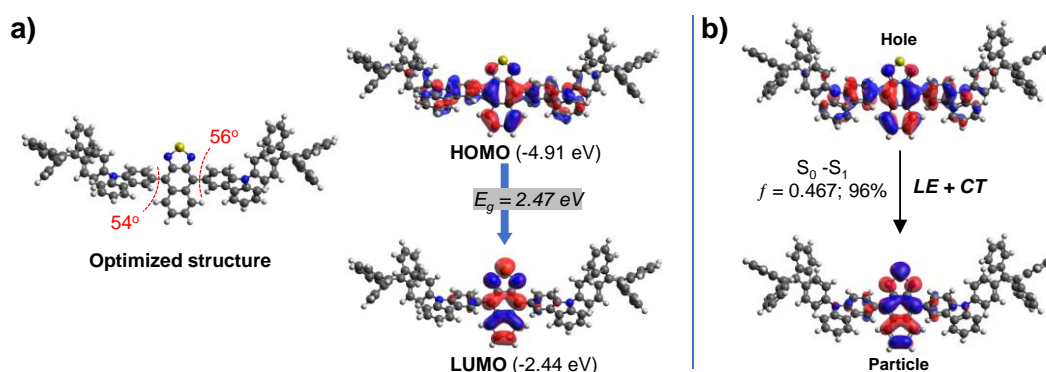


Figure 1. a) The optimized structure and HOMO/LUMO distributions calculated by DFT B3LYP/6-31G(d,p) method. b) The natural transition orbitals (NTOs) of $S_0 \rightarrow S_1$ transition computed by TD-DFT CAM-B3LYP/6-31G(d) method. The percentage is the proportion of transition and f is the oscillator strength.

The photophysical properties of **TPECNz** were studied in solutions, thin film, and solid powder. As shown in Figure 2a, the UV-vis absorption spectrum in diluted toluene solution displays intense absorption peaks in the UV region (295 and 335sh nm) and a much weaker absorption peak at 508 nm attributed to the π - π^* transition of conjugated aromatic backbone and intramolecular charge-transfer (ICT) transition from carbazole donor to Nz acceptor, respectively. Such a much weaker ICT absorption peak ($\epsilon = 17,000 \text{ M}^{-1} \text{ cm}^{-1}$) as compared to the π - π^* absorption peak ($\epsilon = 95,300 \text{ M}^{-1} \text{ cm}^{-1}$) symbolizes a weak electronic coupling between carbazole donor and Nz acceptor parts because of the twisted configuration between them as observed in the optimized structure (Figure 1a).[47] In solution, **TPECNz** exhibited a strong deep-red emission

with the PL spectrum ($\lambda_{em} = 648$ nm) described by a broad band that reflects the corresponding ICT absorption band well, featuring no significant vibronic structure, and a considerably large Stokes shift of 140 nm. The UV-vis absorption and PL spectra of the spin-coated films were similar to those of the diluted solution. Based on the onset energy of this UV-vis spectrum, the optical band gap (E_g^{opt}) was estimated to be 2.04 eV. **TPECNz** in the thin film and solid powder also displayed deep-red emission observed by PL maxima at 668 and 665 nm, respectively (Figure 2b). As listed in Table 1, the **TPECNz** solution shows an excellent absolute PL quantum yield (Φ_{PL}) of 96%, whereas the spin-coated thin film exhibits a red-shifted spectrum with the Φ_{PL} drop to 35% due to intermolecular interactions. However, the emission efficiency of the molecule enhances in the solid power form with a Φ_{PL} of 64% owing to its AIE nature.

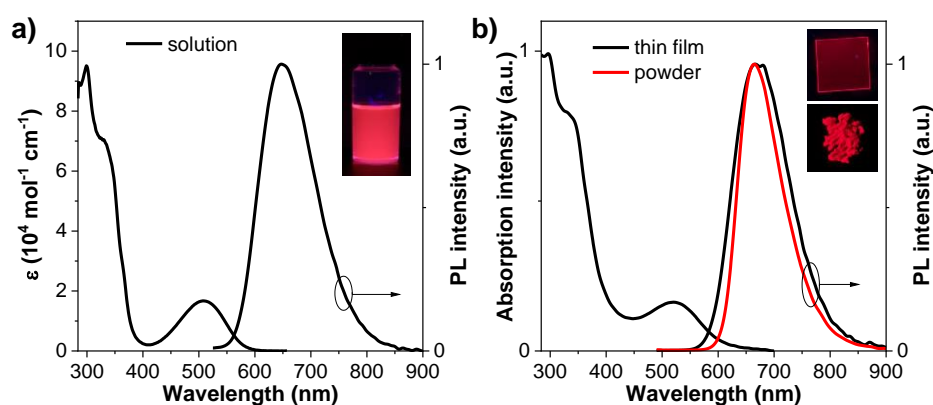


Figure 2. UV-Vis absorption and PL spectra in a) toluene solution ($\sim 1 \times 10^{-5}$ M) and b) thin film spin-coated on fused silica substrates and solid powder (insert: fluorescence images of the solution, thin film, and solid powder under UV light at 356 nm).

To gain more information about the effect of the solvent on the optical properties of **TPECNz**, the absorption and emission behaviors were investigated in several solvents as illustrated in Figure 3a. The results showed that, while UV-vis absorption spectra were nearly unaffected by the nature of the solvent due to the LE nature, the emission spectra exhibited a noticeable positive solvatochromism, with maxima shifting towards longer wavelength with increasing solvent polarities. Particularly, the maximum PL peaks at low polar solvents showed little shifts because of the LE character, whereas the redder shifts of PL maxima apparently occurred in the higher polar solvents due to CT excited state; therefore, the molecule contains both the intrinsic LE and CT excited states or demonstrates HLCT characteristics. Besides, the Stokes shifts between absorption and emission spectra were plotted as a function of solvent polarity function (f) corresponding to the Lippert-Mataga model which defines the interactions between the solvent and dipole moment of the chromophore (Figure 3b). The Lippert–Mataga plot showed two linear

slopes indicating the presence of two different excited states in the molecule. In the high-polarity region, the excited-state dipole moment (μ_e) was 19.04 D, which was close to that of typical CT molecule 4-(N,N-dimethylamino)benzonitrile ($\mu_e = 23$ D),[55] suggesting a CT state-dominated character in high-polarity solvents. Besides, in the low-polarity region, the μ_e value was 5.49 D, which is slightly higher than its ground-state dipole moment ($\mu_g = 1.30$ D) estimated using B3LYP/6-31G(d, p) calculation. Nevertheless, this value was significantly smaller than that of the high-polarity region, indicating that the S_1 state in low-polarity solvents contained both CT and LE components simultaneously, which underwent interstate coupling forming a new HLCT emissive state. Additionally, transient PL decay spectra of **TPECNz** in solvents of different polarities showed single exponential decay in nanosecond ranges (Figure 3c), signifying that the excited state responsible for the PL emission originates from the hybridization between LE and CT excited states or HLCT state, not a simple mix-up of the two states.[56]

Furthermore, to further understand the Φ_{PL} of the molecule in solution and thin film, the radiative rate constant (k_r) and non-radiative rate constant (k_{nr}) were calculated from the Φ_{PL} values and PL lifetime (τ) according to the following equations.

$$k_r = \frac{\Phi_{PL}}{\tau}$$

$$\Phi_{PL} = \frac{k_r}{k_r + k_{nr}}$$

As can be seen from Table 1, the k_r of **TPECNz** in solution is relatively larger than the k_{nr} , consistent with the result of its high Φ_{PL} in the solution. The k_r and k_{nr} of **TPECNz** in thin film are somewhat similar, still, this k_{nr} is significantly higher than the k_{nr} of solution, explaining the drop of Φ_{PL} in thin film as compared to the value in the solution. However, the moderate Φ_{PL} of its thin-film still makes **TPECNz** suitable for the deep red OLEDs

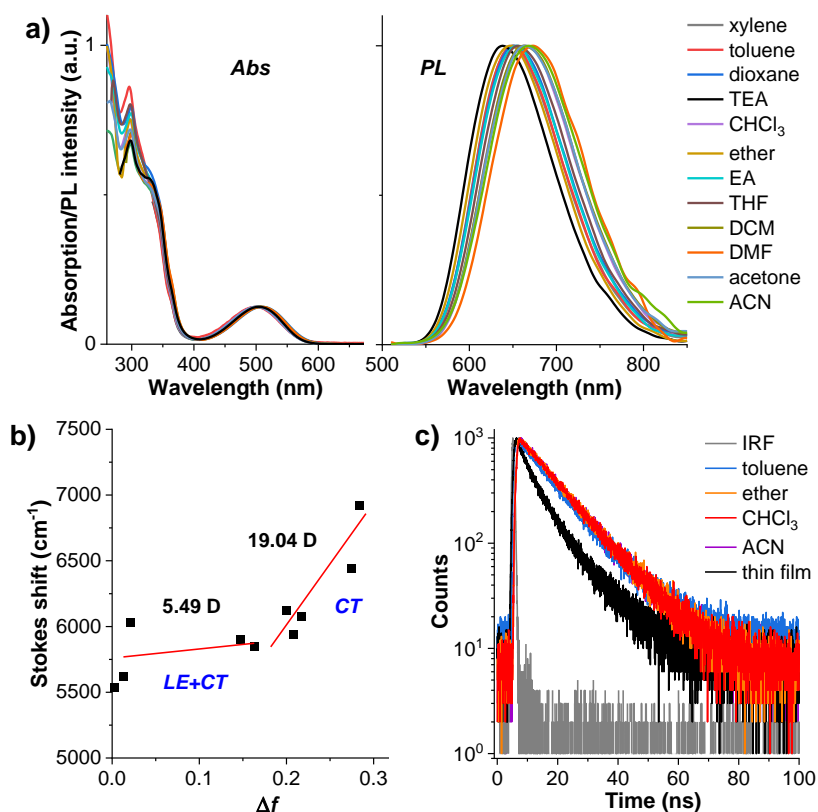


Figure 3. a) Normalized UV-vis absorption/PL spectra in different solvents. b) Lippert–Mataga plot of Stokes shift vs solvent polarity function (Δf). c) Transient PL decay traces in various solvents and thin film.

In addition, the AIE characteristic of **TPECNz** was further investigated by observing its PL emissions in water/THF mixtures with different water fractions ($f_w = 0-95\%$). In such diverse solvent mixtures, the molecule will demonstrate different degrees of aggregation since it can dissolve really well in THF but is insoluble in water, resulting in colloidal nanoaggregates being formed in solutions with high water contents. As shown in Figures 4a and 4b, in the pure THF, **TPECNz** deep-red emission color with the PL peaked at 658 nm. With the increase of f_w , the PL emission maxima suddenly dropped. At $f_w = 40\%$, PL intensity reached the lowest point, as well as the PL peak being red-shifted. Such changes in the emission aspects could be ascribed to the ICT emission characteristics of the fluorophores, which often feature a red-shifted PL emission and a weakened emission intensity with increasing solvent polarity. As the f_w was further increased to 95%, the PL emissions were intensified and blue-shifted, which could be attributed to the formation of nanoaggregates and suppression of the ICT process. This finding proves that both **TPECNz** is AIE-active fluorophore.

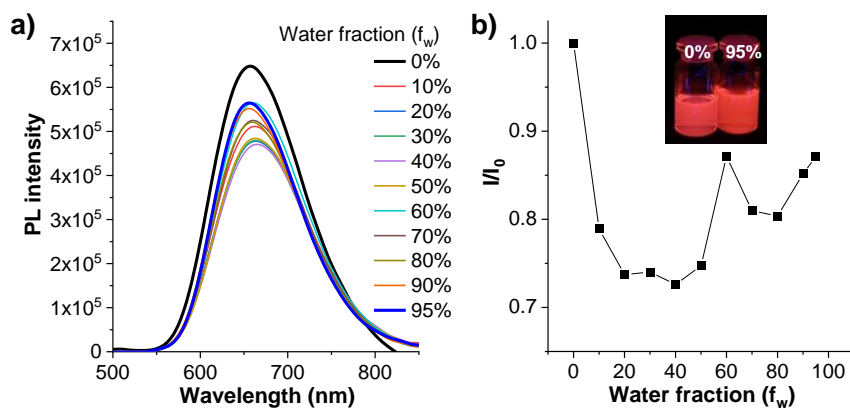


Figure 4. a) PL spectra in THF-water mixtures (5 μ M) with different water fractions (f_w). b) Plot of relative PL intensity (I/I_0) vs % of water fraction (f_w) (insert: photographs of the solutions @ f_w of 0% and 95% taken under UV illumination).

The thermal property of **TPECNz** was studied by the thermogravimetric analysis (TGA) and differential scanning calorimetry (DSC) methods under an N_2 atmosphere at a scanning rate of $10\text{ }^\circ\text{C min}^{-1}$. As displayed in Figure 5a, the compound has high thermal stability with a decomposition temperature at 5% weight loss (T_{5d}) of $498\text{ }^\circ\text{C}$, glass transition temperature (T_g) of $236\text{ }^\circ\text{C}$, and melting temperature (T_m) of $376\text{ }^\circ\text{C}$. The high T_g may enhance the morphological thin film stability, electrical conductance, and film integrity of **TPECNz** during device fabrication. While the high T_m suggests that **TPECNz** can withstand the latent heat generated during the device fabrication and operation. These results signaled that **TPECNz** may be suitable for optoelectronic devices. The electrochemical behavior of **TPECNz** was analyzed by cyclic voltammetry (CV) and differential plus voltammetry (DPV) in CH_2Cl_2 containing $0.1\text{ M } n\text{-Bu}_4\text{NPF}_6$ as a supporting electrolyte. As illustrated in Figure 5b, the molecule shows multiple quasi-reversible oxidation and reduction behaviors in the potential window from -1.5 eV to 2.0 eV . The reduction wave appeared at half-wave potential ($E_{1/2}$) of -1.26 eV assigned to the reduction of an electron-deficient Nz core as observed in the calculated LUMO orbital.[39] The first oxidation wave occurred at $E_{1/2}$ of 1.05 eV ascribed to the oxidation of π -conjugated backbone along Nz core and end-capped carbazole moieties as seen in computed HOMO orbital, while the second oxidation wave at $E_{1/2}$ of 1.47 eV attributed to the oxidation of π -conjugated TPE-carbazole fragment as depicted in calculated HOMO-1 orbital. In addition, the oxidation and reduction onsets of **TPECNz** were 1.00 eV and -1.17 eV , respectively. Hence, the electrochemical energy gap (E_g^{ele}) defined as the difference between the oxidation and reduction onset potentials was calculated to be 2.17 eV , which was slightly higher than the E_g^{opt} estimated from the UV-vis absorption onset (Table 1). The HOMO energy level was calculated from the oxidation onset potential to be -5.44 eV . Further,

the calculated LUMO energy level was found to be -3.40 eV. The relatively low LUMO level of **TPECNz** is conceivably associated with a high electron deficiency of the Nz moiety originating from its localized distribution of electrons and the high electronegativities of the N and S atoms, whereas its high HOMO level is attributed to electron-donating property of the attached carbazoles and the π -conjugation of the carbazole-Nz-carbazole fragment. Such proper energy levels will benefit the efficient charge injections from the electrodes in OLEDs.

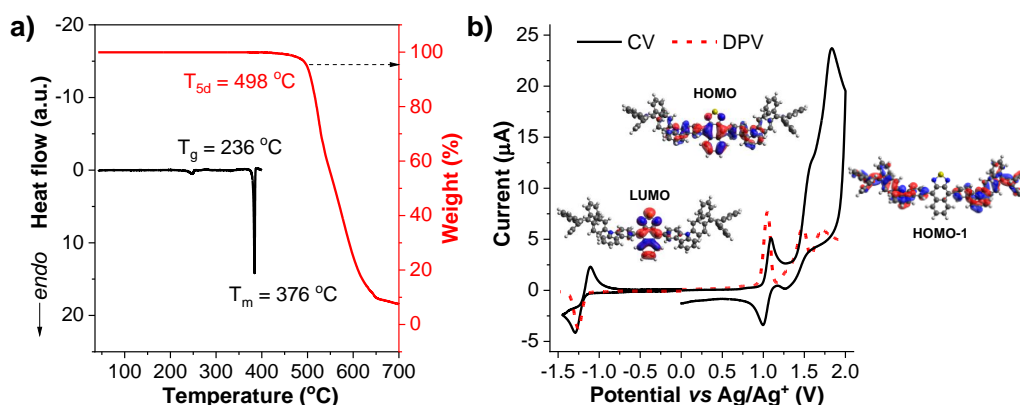


Figure 5. a) DSC and TGA thermograms measured at a heating rate of $10\text{ }^{\circ}\text{C min}^{-1}$ under N_2 flow. c) Cyclic voltammogram (CV) and differential pulse voltammogram (DPV) analyzed in dry CH_2Cl_2 at a scan rate of 50 mV s^{-1} under an argon atmosphere (insert: HOMO/HOMO-1/LUMO orbitals).

To evaluate charge-carrier mobility in **TPECNz**, hole (μ_h) and electron (μ_e) mobilities were initially measured using metal-insulator-semiconductor (MIS) diodes in combination with charge extraction in linearly increasing voltage (CELIV) or MIS-CELIV technique.[57–60] Electron- and hole-only MIS devices were fabricated with the structures of indium tin oxide (ITO)/magnesium fluoride (MgF_2) (20 nm)/**TPECNz** (100 nm)/lithium fluoride (LiF) (1 nm)/aluminum (Al) (100 nm) and ITO/ MgF_2 (20 nm)/**TPECNz** (100 nm)/molybdenum trioxide (MoO_3) (6 nm)/Al (100 nm), respectively (Figure 6a), where in MgF_2 layer was employed as an insulator. During the measurements, varied maximum voltages were applied during the pulse for extracting the charges while keeping the pulse duration and off set voltage of 10 μs and 5 V for electron-only MIS device and 15 μs and -5 V hole-only MIS device, respectively, and their MIS-CELIV signal transient plots as a function of time are shown in Figures 6c and 6d. As the applied voltage increased, it was found that the transient peak shifted to slightly shorter times indicating an increasing carrier mobility. The hole and electron mobilities (μ) were calculated and plotted as a function of electric field ($E^{1/2}$). As illustrated in Figure 6b, the mobility (μ) of both holes and electrons is electric field dependent and gradually increases on increasing the electric field, which is explained as the Poole-

Frenkel effect obeying the relationship, $\log \mu \propto E^{1/2}$.^[57] The measured mobilities of the holes (μ_h) and electrons (μ_e) of **TPECNz** thin film at $950 \text{ (V cm}^{-1}\text{)}^{1/2}$ electric field were 4.42×10^{-6} and $1.50 \times 10^{-5} \text{ cm}^2 \text{ V}^{-1} \text{ s}^{-1}$, respectively. This result suggested that **TPECNz** was ambipolar material with the mobility of electrons somewhat greater than that of holes. Such pronounced ability to transport electrons of **TPECNz** could be accredited to a strong electron affinity of the Nz core, while its ability to transport holes could be derived from the attached carbazole moieties.

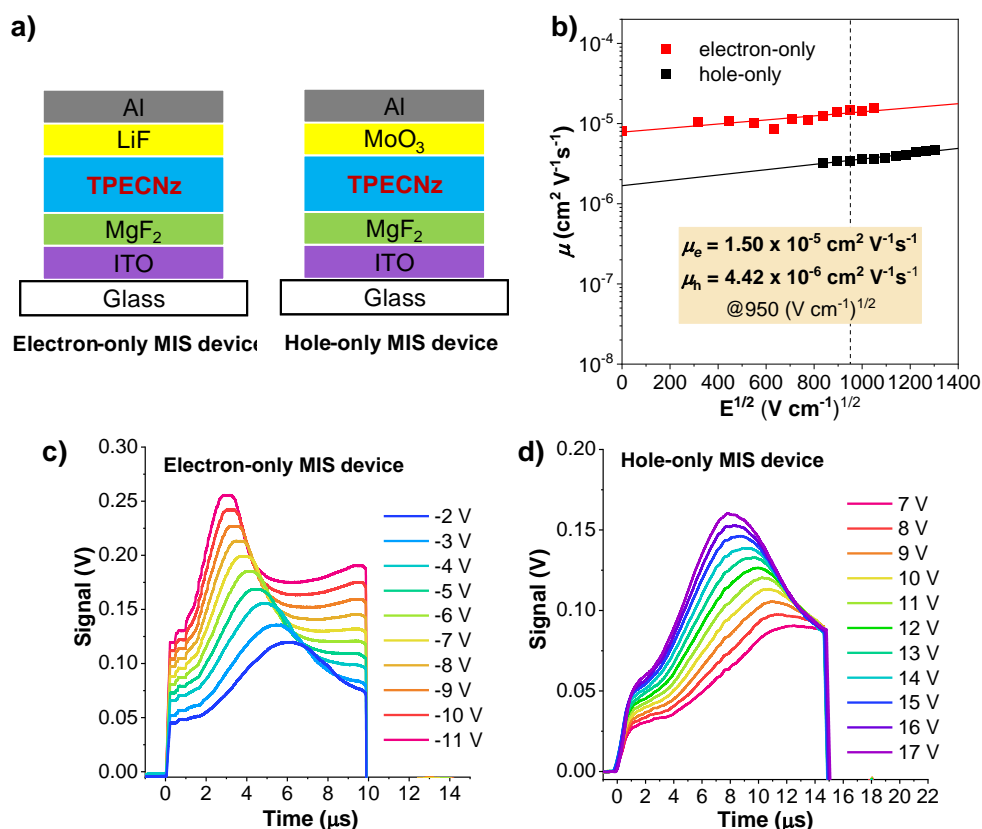


Figure 6. a) Schematic structure of the hole-only and electron-only MIS devices. b) Electric-field dependence of the hole and electron mobilities. Transient signals at different applied maximum voltages for c) electron-only MIS device and d) hole-only MIS device.

Table 1: Optical and physical data of **TPECNz**.

λ_{PL} (nm) sol ^a /film ^b /solid ^c	τ (ns) ^d sol ^a /film ^b	Φ_{PL} (%) ^e sol ^a /film ^b /solid ^c	k_r/k_{nr} (10 ⁷ s ⁻¹) ^a	k_r/k_{nr} (10 ⁷ s ⁻¹) ^b	$E_{1/2}$ vs Ag/Ag ⁺ (V) ^f	$E_g^{\text{opt}}/E_g^{\text{ele}}$ (eV) ^g	HOMO/LUMO (eV) ^h
648/668/ 664	13.4/11.1	96/35/64	7.16/0.30	3.15/5.86	-1.26, 1.05, 1.47, 1.72	2.04/2.17	-5.44/-3.40

^aMeasured in diluted toluene solution (1×10^{-5} M); ^bMeasured in thin film; ^cMeasured in solid powder; ^dTransient PL decay lifetime with excitation at 475 nm; ^eAbsolute PL quantum yield measured by an integrating sphere; ^fObtained from differential pulse voltammetry (DPV) peak;

^gBand-gap energy from UV-absorption (E_g^{opt}) and electrochemical (E_g^{ele}) results; ^hCalculated from HOMO (eV) = - (4.44 + $E_{\text{onset}}^{\text{ox}}$) and LUMO (eV) = HOMO + E_g^{opt} .

To evaluate the electroluminescent (EL) performance of **TPECNz**, non-doped OLED employing **TPECNz** as an emissive layer (EML) was fabricated through thermal evaporation the optimized device configuration of ITO/1,4,5,8,9,11-hexaaza-triphenylene-hexacarbonitrile (HAT-CN) (6 nm)/N,N'-bis(naphthalen-1-yl)-N,N'-bis(phenyl)-benzidine (NPB) (30 nm)/tris(4-carbazoyl-9-ylphenyl)-amine (TCTA) (10 nm)/**TPECNz** (60 nm)/1,3,5-tris(1-phenyl-1H-benzimidazol-2-yl)benzene (TPBi) (40 nm)/LiF (1 nm)/Al (100 nm), in which ITO and Al served as anode and cathode, respectively (Figure 7a). Herein, HAT-CN and LiF were used as the hole- and electron-injection layers, respectively, NPB and TPBi were applied as the hole- and electron-transporting layers, respectively, and TCTA owing to its high-lying LUMO energy level (LUMO = 2.3 eV) and low electron mobility was utilized as an electron-blocking layer.[61] Owing to a narrow band gap stemming from its strong D-A characteristic, **TPECNz**-based non-doped OLED successfully displayed deep red emission with a maximum EL peak at 659 nm and Commission Internationale de L'Eclairage (CIE) coordinates of (0.664, 0.335), which were very close to the standard red CIE coordinates of (0.67, 0.33).[62] The device demonstrated high emission stability with EL spectra under different operating voltages (6-9 V) revealing an unchanged profile with a single emission band (Figure 7b), indicating the recombination zone of the excitons confined inside the EML. No emission peaks at low wavelengths from the supporting layers (NPB at 440 nm,[63] TCTA at 410 nm,[64] and TPBi at 390 nm[65]) and at longer wavelengths due to the excimer/excimer emissions at the interfaces of NPB-TCTA/EML and EML/TPBi were observed, signifying that the OLED possessed a well-balanced electron and hole transport. Moreover, due to efficient ambipolar charge-carrier-transporting property of **TPECNz** EML and good charge balance in the device, the non-doped OLED was turned on at a low voltage of 3.2 V and achieved decent device EL performance as presented in Figures 7c and 7d. The device exhibited a maximum luminance (L_{max}) of 7430 cd m⁻², a maximum external quantum efficiency (EQE_{max}) of 3.32%, and a maximum luminance efficiency (LE_{max}) of 2.87 cd A⁻¹, with a little efficiency roll-off of 9% at 1000 cd m⁻². Furthermore, its exciton utilization efficiency (EUE) was calculated using $\text{EUE} = \text{EQE}/(\eta_{\text{out}} \times \eta_{\text{rec}} \times \Phi_{\text{PL}})$ (light outcoupling efficiency: $\eta_{\text{out}} = 20\%$, Φ_{PL} in a thin film = 35%, and charge recombination: $\eta_{\text{rec}} = 100\%$) to be 47%. This EUE was higher than the 25% theoretical upper limit of spin statistics for typical fluorescent emitters, indicating that the triplet excitons have been utilized *via* an HLCT mechanism to contribute to the EL in this device.

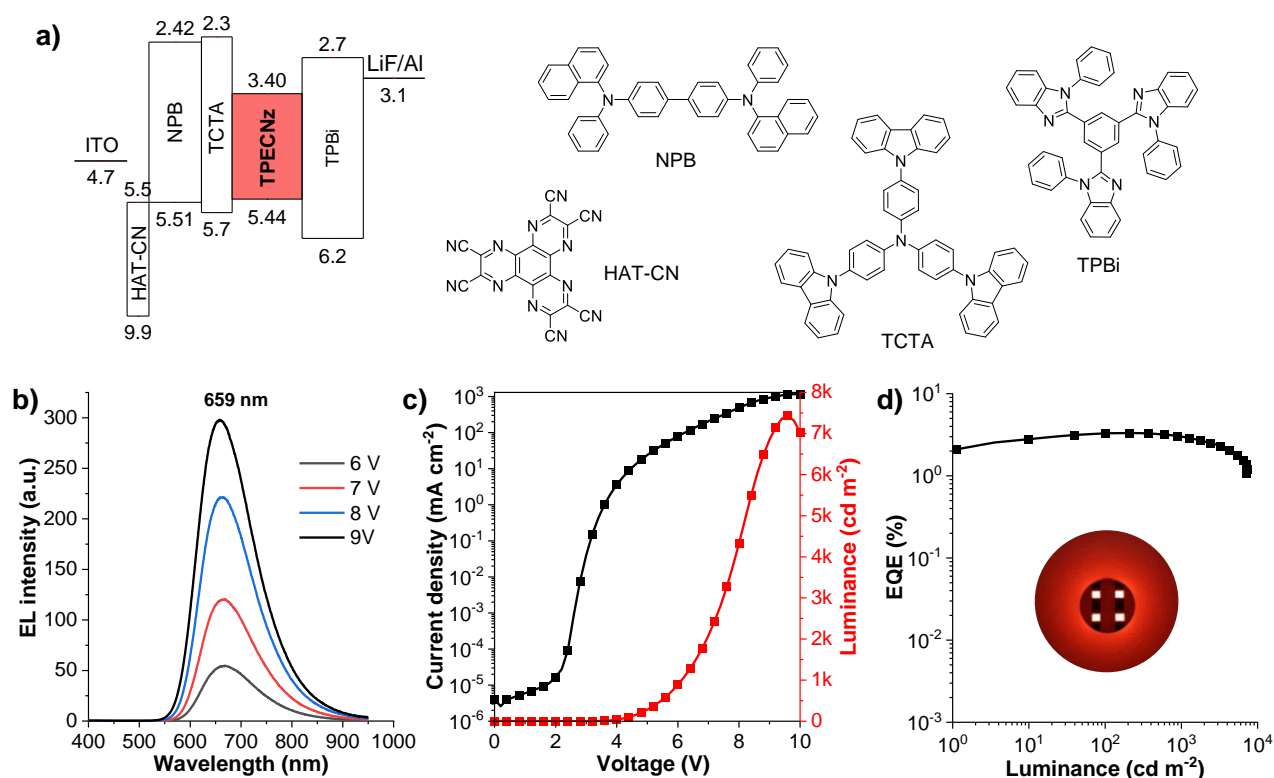


Figure 7. a) Schematic energy diagram of OLED and organic materials used in the device. b) EL spectra at various applied voltages. c) Current density-voltage-luminance (J - V - L) characteristics. d) External quantum efficiency-luminance (EQE - L) plot (insert: photograph of OLED under operation).

Conclusion

In summary, a new D-A-D type fluorophore as a deep-red emitter has been designed and synthesized by exploiting a strong electron-accepting naphtho[2,3-*c*][1,2,5]thiadiazole (Nz) as A unit and N-(4-(1,2,2-triphenylvinyl)phenyl)-carbazole as D unit. The integration of 4-(1,2,2-triphenylvinyl)phenyl (TPE) moiety as an AIE luminogen helped to provide the fluorophore with AIE feature, while its D-A-D structure with a proper twist angle (54-56°) between the Nz acceptor and carbazole donor promotes a state mixing between close-lying LE and CT states or HLCT property. The combined feature of HLCT and AIE was clearly confirmed by solvatochromic study, emission in THF-water investigation, and theoretical calculations. These synergetic properties could benefit for effective utilization of excitons in the OLED. A collaborative consequence of its D-A-D type structure, a strong electron affinity of Nz unit, and electron donating and hole-transporting properties of carbazole nurtured the molecule to exhibit an intense deep red emission with decent PL quantum yield, superior thermal property, and ambipolar charge-carrier-transporting property with a good balance of mobility of electron and

hole, which were desirable properties for OLED application. It was efficiently utilized as a non-doped emitter in OLEDs. The device presented strong deep red electroluminescent (EL) emission (peak at 659 nm and CIE coordinates of (0.664, 0.335)) with a maximum luminance of 7430 cd m⁻², EQE_{max} of 3.32%, and EUE of 47%. This work successfully established that an ambipolar D–A–D type fluorophore having combined AIE-HLCT features could be a promising design to develop future deep red or near-infrared OLEDs.

Experimental

Materials and Methods

All chemical reagents and solvents were provided by commercial sources and used without further purification. ¹H-NMR and ¹³C-NMR spectra were recorded with Bruker AVANCE III HD 600 (600 MHz-¹H, 151 MHz-¹³C) using CDCl₃ as a solvent containing TMS as an internal standard. High-resolution mass spectrometry (HRMS) analysis was performed using either Bruker LC-Quadrupole-Time-of Flight Tandem Mass Spectrometer or Bruker Autoflex MALDI-TOF mass spectrometer. UV–vis spectra were performed using Perkin Elmer Lambda 1050 UV/Vis/NIR spectrometer. Luminescence emission spectra and lifetime were analyzed using Edinburgh Instruments FLS980 Spectrometer. Absolute PL quantum yield (Φ_{PL}) was measured using a calibrated integrating sphere incorporated with Edinburgh Instruments FLS980 Spectrometer. Electrochemical studies were carried out using Autolab PGSTA101 potentiostat equipped with three electrodes (Pt, glassy carbon, and Ag/AgCl) in dry CH₂Cl₂ containing 0.1M *n*-Bu₄NPF₆ as a supporting electrolyte under argon. Thermogravimetric analysis (TGA) and differential scanning calorimetry (DSC) were recorded using Rigaku STA8122 Thermogravimetric Analyzer and PerkinElmer DSC 8500 Lab System, respectively. Melting points were measured using a Krüss KSP1N melting point meter and uncorrected.

Quantum chemical calculations were executed using the Gaussian 16 package.[66] Density functional theory (DFT) calculations at the B3LYP level with 6-31G (d,p) basis set were performed to realize the ground state geometry, HOMO and LUMO distributions, and HOMO, LUMO energy levels. Natural transition orbitals (NTOs) were calculated for the excited states using time-dependent (TD)-DFT calculations at the CAM-B3LYP/6-31G(d) level of theory.

Device Fabrication and Testing

The patterned ITO-coated glass substrate with a sheet resistance of 12 Ω sq⁻¹ was pre-cleaned carefully and cured with UV/O₃ for 20 min. The OLED with an active diode area of 0.04 cm⁻² was

fabricated using a Kurt J. Lasker mini SPECTROS 100 thin film deposition system under vacuum conditions with a base pressure lower than 1×10^{-5} bar and thermal evaporation rate of 0.2 - 0.3 \AA s^{-1} for MgF₂, HATCN, NPB, TCTA, TPECNz and TPBi, 0.05-0.1 \AA s^{-1} for LiF, and about 1 \AA s^{-1} for Al layer. The thickness of each layer was monitored by a quartz oscillator thickness sensor. All devices were measured without encapsulation under an ambient atmosphere at room temperature. They were analyzed by Keithley 2400 source meter, a Hamamatsu Photonics PMA-12 multi-channel analyzer, and an integrating sphere equipped with a Hamamatsu Photonics C9920-12 EQE Measurement System. The hole and electron mobility were investigated using MIS-CELIV measurement. A pulse delay generator (Stanford Research System DG535) and a single channel arbitrary/function generator (AFG 3021B) were used to generate the CELIV triangle pulse with adjustable voltage slope and offset, as well as amplified the signal by WMA-320 high voltages amplifier. For photo-CELIV, a delay generator (Stanford Research System DG535) was also used for pulse synchronization along with a LED-driver (THORLABS, LEDD1B). The signal was recorded by a 3 series mixed domain oscilloscope (Tektronix, MDO32).

Synthesis of 9-(4-(1,2,2-triphenylvinyl)phenyl)-9H-carbazole (2): A mixture of **1** (2.00 g, 4.86 mmol), carbazole (2.44 g, 14.58 mmol), K₃PO₄ (5.17 g, 24.313 mmol), \pm trans-1,2-diamino cyclohexane (1.46 mL, 12.17 mmol) and CuI (1.85 g, 9.72 mmol) in dried toluene (50 mL) was degassed with N₂ for 10 min. The reaction mixture was stirred at reflux under N₂ atmosphere for 18 h. After being cooled to room temperature, it was diluted with water (100 mL) and extracted with CH₂Cl₂ (50 mL x 3). The combined organic layer was washed with water, brine solution, dried over anhydrous Na₂SO₄, filtered, and concentrated under reduced pressure. The crude product was then purified by column chromatography over silica gel eluting with CH₂Cl₂:hexane (1:4) to give white solids (2.11 g, 87%). ¹H NMR (600 MHz, CDCl₃) δ 8.12 (d, *J* = 7.7 Hz, 2H), 7.40 (t, *J* = 7.8 Hz, 2H), 7.34 (d, *J* = 8.2 Hz, 2H), 7.28 (t, *J* = 8.0 Hz, 4H), 7.24 (d, *J* = 8.1 Hz, 2H), 7.21 – 7.07 (m, 15H). ¹³C NMR (151 MHz, CDCl₃) δ 143.55, 143.41, 143.30, 142.94, 141.84, 140.74, 140.12, 135.68, 132.67, 131.42, 131.37, 131.32, 127.85, 127.77, 127.72, 126.73, 126.69, 126.62, 126.12, 125.83, 123.32, 120.25, 119.84, 109.80. HRMS APCI-TOF *m/z*: [M + H]⁺ calcd for C₃₈H₂₈N, 498.2216; found, 498.2233.

Synthesis of 3-(4,4,5,5-tetramethyl-1,3,2-dioxaborolan-2-yl)-9-(4-(1,2,2-triphenylvinyl)phenyl)-9H-carbazole (3): A round bottom flask containing a solution of **2** (1.81 g, 3.63 mmol) in THF (200 mL) was covered with aluminum foil and cooled in an ice bath. A solution of NBS (646 mg, 3.63 mmol) in THF (100 mL) was added as dropwise into the solution

for a period of 2 h, while monitoring the reaction by TLC with CH₂Cl₂:hexane (1:4). The reaction mixture was quenched with water (100 mL) and extracted with CH₂Cl₂ (50 mL x 3). The combined organic layer was washed with water, brine solution, dried over anhydrous Na₂SO₄, filtered, and concentrated under reduced pressure. The residue was recrystallized in CH₂Cl₂/methanol to obtain white solids (1.34 g, 2.32 mmol). HRMS APCI-TOF *m/z*: [M + H]⁺ calcd for C₃₈H₂₈N, 498.2216; found, 498.2217; [M + H]⁺ calcd for C₃₈H₂₇BrN, 576.1321; found, 576.1331; [M + H]⁺ calcd for C₃₈H₂₆Br₂N, 654.0427; found, 654.0438.

A mixture of a crude product (1.00 g, 1.74 mmol), bis(pinacolato)diboron (881 mg, 3.47 mmol), KOAc (2.04 g, 20.81 mmol), and Pd(dppf)Cl₂ (70.8 mg, 0.087 mmol) in dried toluene (50 mL) was degassed with N₂ for 10 min. The reaction mixture was stirred at a refluxing temperature under N₂ atmosphere for 48 h. After being cooled to room temperature, it was diluted with water (100 mL) and extracted with CH₂Cl₂ (50 mL x 3). The combined organic layer was washed with water, brine solution, dried over anhydrous Na₂SO₄, filtered, and concentrated under reduced pressure. The crude product was then purified by column chromatography over silica gel eluting with CH₂Cl₂:hexane (3:7) to give **3** as white solids (928 mg, 55% over two steps). ¹H NMR (600 MHz, CDCl₃) δ 8.61 (s, 1H), 8.15 (d, *J* = 7.7 Hz, 1H), 7.85 (d, *J* = 8.2 Hz, 1H), 7.39 (t, *J* = 7.7 Hz, 1H), 7.34 – 7.22 (m, 7H), 7.22 – 7.04 (m, 15H), 1.40 (s, 12H). ¹³C NMR (151 MHz, CDCl₃) δ 143.54, 143.38, 143.24, 143.13, 142.88, 141.95, 140.91, 140.13, 135.48, 132.70, 132.35, 131.43, 131.38, 131.32, 127.88, 127.77, 127.73, 127.70, 126.75, 126.72, 126.65, 126.15, 125.86, 123.54, 123.06, 120.50, 120.25, 109.83, 109.19, 83.66, 24.95. HRMS APCI-TOF *m/z*: [M + H]⁺ calcd for C₄₄H₃₉BNO₂, 624.3068; found, 624.3078.

Synthesis of 4,9-bis(9-(4-(1,2,2-triphenylvinyl)phenyl)-9H-carbazol-3-yl)naphtho[2,3-c][1,2,5]thiadiazole (TPECNz): A mixture of **3** (834 mg, 1.34 mmol), 4,9-dibromonaphtho[2,3-c][1,2,5]thiadiazole (200 mg, 0.58 mmol), Pd(PPh₃)₄ (80.6 mg, 0.070 mmol) and 2M Na₂CO₃ (8.7 mL, 17.44 mmol) in THF (50 mL) was degassed with N₂ for 3 min. The reaction mixture was stirred at a refluxing temperature under N₂ atmosphere for 48 h. After being cooled to room temperature, it was diluted with water (100 mL) and extracted with CH₂Cl₂ (50 mL x 3). The combined organic layer was washed with water, brine solution, dried over anhydrous Na₂SO₄, filtered, and concentrated under reduced pressure. The crude product was then purified by column chromatography over silica gel eluting with CH₂Cl₂:hexane (3:7), then recrystallized in CH₂Cl₂/methanol mixture to attain red solids (396.0 mg, 58%). M.p. >360 °C. ¹H NMR (600 MHz, CDCl₃) δ 8.43 (s, 2H), 8.15 (td, *J* = 7.1, 3.5 Hz, 4H), 7.74 (dd, *J* = 8.3, 1.7 Hz, 2H), 7.60 (d, *J* = 8.3 Hz, 2H), 7.45 (t, *J* = 7.6 Hz, 2H), 7.41 (t, 6H), 7.35 (dd, *J* = 7.2, 3.2 Hz, 2H), 7.30 (d, *J* = 8.3 Hz, 6H), 7.24 – 7.07 (m, 30H). ¹³C NMR (151 MHz, CDCl₃) δ 152.04, 143.54, 143.40, 143.29,

143.19, 141.93, 141.27, 140.62, 140.10, 135.60, 132.78, 132.46, 131.43, 131.38, 131.31, 130.75, 129.14, 128.16, 127.87, 127.81, 127.72, 127.43, 126.78, 126.71, 126.63, 126.22, 126.17, 123.56, 123.35, 123.21, 120.53, 120.11, 110.03, 109.89. HMRS MALDI-TOF m/z : $[M]^+$ calcd for $C_{86}H_{56}N_4S$, 1176.4226; found, 1176.4221.

Supporting Information

Copies of 1H -NMR, ^{13}C -NMR, HRMS spectra of the synthesized compounds.

Acknowledgements

We thank VISTEC for the scholarship support for S. A. and A. S.

Funding

This work was financially supported by the National Research Council of Thailand (NRCT) (no. N42A650196).

References

- (1) Zhao, M.; Guo, Y. S.; Xu, W. N.; Zhao, Y. F.; Xie, H. Y.; Li, H. J.; Chen, X. F.; Zhao, R. S.; Guo, D. S. *TrAC - Trends Anal. Chem.* **2020**, *122*, 115704.
- (2) Gomes, L. J.; Carrilho, J. P.; Pereira, P. M.; Moro, A. J. *Sensors* **2023**, *23*, 471.
- (3) Laramie, M. D.; Levitz, A.; Henary, M. *Sensors Actuators, B Chem.* **2017**, *243*, 1191.
- (4) Shen, Q.; Wang, S.; Yang, N. Di; Zhang, C.; Wu, Q.; Yu, C. *J. Lumin.* **2020**, *225*, 117338.
- (5) Feng, X.; Wei, L.; Liu, Y.; Chen, X.; Tian, R. *Adv. Healthc. Mater.* **2023**, 2300537.
- (6) Miao, W.; Guo, X.; Yan, X.; Shang, Y.; Yu, C.; Dai, E.; Jiang, T.; Hao, E.; Jiao, L. *Chem. - A Eur. J.* **2023**, *29*, e202203832.
- (7) Zhang, F.; Tang, B. Z. *Chem. Sci.* **2021**, *12*, 3377.
- (8) Li, J.; Dong, Y.; Wei, R.; Jiang, G.; Yao, C.; Lv, M.; Wu, Y.; Gardner, S. H.; Zhang, F.; Lucero, M. Y.; Huang, J.; Chen, H.; Ge, G.; Chan, J.; Chen, J.; Sun, H.; Luo, X.; Qian, X.; Yang, Y. *J. Am. Chem. Soc.* **2022**, *144*, 14351.
- (9) Chen, L.; Chen, M.; Zhou, Y.; Ye, C.; Liu, R. *Front. Chem.* **2021**, *9*, 629062.
- (10) Minotto, A.; Haigh, P. A.; Łukasiewicz, Ł. G.; Lunedei, E.; Gryko, D. T.; Darwazeh, I.; Cacialli, F. *Light Sci. Appl.* **2020**, *9*, 70.
- (11) Patil, D.; Jadhav, M.; Avhad, K.; Gawale, Y.; Sekar, N. *J. Lumin.* **2018**, *204*, 436.
- (12) Aoki, R.; Komatsu, R.; Goushi, K.; Mamada, M.; Ko, S. Y.; Wu, J. W.; Placide, V.; D'Aléo, A.; Adachi, C. *Adv. Opt. Mater.* **2021**, *9*, 2001947.
- (13) Wan, Q.; Tong, J.; Zhang, B.; Li, Y.; Wang, Z.; Tang, B. Z. *Adv. Opt. Mater.* **2020**, *8*, 1901520.
- (14) Ye, H.; Kim, D. H.; Chen, X.; Sandanayaka, A. S. D.; Kim, J. U.; Zaborova, E.; Canard, G.; Tsuchiya, Y.; Choi, E. Y.; Wu, J. W.; Fages, F.; Bredas, J. L.; D'Aléo, A.; Ribierre, J. C.; Adachi, C. *Chem. Mater.* **2018**, *30*, 6702.
- (15) Xiao, Y.; Wang, H.; Xie, Z.; Shen, M.; Huang, R.; Miao, Y.; Liu, G.; Yu, T.; Huang, W.

- Chem. Sci.* **2022**, *13*, 8906.
- (16) Therdkatanyuphong, P.; Chasing, P.; Kaiyasuan, C.; Boonnab, S.; Sudyoasuk, T.; Promarak, V. *Adv. Funct. Mater.* **2020**, *30*, 2002481.
 - (17) Lee, W. W. H.; Zhao, Z.; Cai, Y.; Xu, Z.; Yu, Y.; Xiong, Y.; Kwok, R. T. K.; Chen, Y.; Leung, N. L. C.; Ma, D.; Lam, J. W. Y.; Qin, A.; Tang, B. Z. *Chem. Sci.* **2018**, *9*, 6118.
 - (18) Lo, Y. C.; Yeh, T. H.; Wang, C. K.; Peng, B. J.; Hsieh, J. L.; Lee, C. C.; Liu, S. W.; Wong, K. T. *ACS Appl. Mater. Interfaces* **2019**, *11*, 23417.
 - (19) Caspar, J. V.; Kober, E. M.; Sullivan, B. P.; Meyer, T. J. *J. Am. Chem. Soc.* **1982**, *104*, 630-632.
 - (20) Zampetti, A.; Minotto, A.; Cacialli, F. *Adv. Funct. Mater.* **2019**, *29*, 201807623.
 - (21) Liu, J. F.; Wang, X. Q.; Yu, Y. J.; Zou, S. N.; Yang, S. Y.; Jiang, Z. Q.; Liao, L. S. *Org. Electron.* **2021**, *91*, 106088.
 - (22) Malina, I.; Kampars, V.; Turovska, B.; Belyakov, S. *Dye. Pigment.* **2017**, *139*, 820.
 - (23) Sugihara, Y.; Inai, N.; Taki, M.; Baumgartner, T.; Kawakami, R.; Saitou, T.; Imamura, T.; Yanai, T.; Yamaguchi, S. *Chem. Sci.* **2021**, *12*, 6333.
 - (24) Tang, X.; Li, X. L.; Liu, H.; Gao, Y.; Shen, Y.; Zhang, S.; Lu, P.; Yang, B.; Su, S. J.; Ma, Y. *Dye. Pigment.* **2018**, *149*, 430.
 - (25) Kumsampao, J.; Chaiwai, C.; Chasing, P.; Chawanpunyawat, T.; Namuangruk, S.; Sudyoasuk, T.; Promarak, V. *Chem. - An Asian J.* **2020**, *15*, 3029.
 - (26) Redon, S.; Eucat, G.; Ipuay, M.; Jeanneau, E.; Gautier-Luneau, I.; Ibanez, A.; Andraud, C.; Bretonnière, Y. *Dye. Pigment.* **2018**, *156*, 116.
 - (27) Rémond, M.; Hwang, J.; Kim, J.; Kim, S.; Kim, D.; Bucher, C.; Bretonnière, Y.; Andraud, C.; Kim, E. *Adv. Funct. Mater.* **2020**, *30*, 202004831.
 - (28) Li, Y.; Zhu, H.; Wang, X.; Cui, Y.; Gu, L.; Hou, X.; Guan, M.; Wu, J.; Xiao, Y.; Xiong, X.; Meng, X.; Hong, X. *CCS Chem.* **2022**, *4*, 3735.
 - (29) Essam, Z. M.; Ozmen, G. E.; Setiawan, D.; Hamid, R. R.; Abd El-Aal, R. M.; Aneja, R.; Hamelberg, D.; Henary, M. *Org. Biomol. Chem.* **2021**, *19*, 1835.
 - (30) Zhao, F.; Sun, T.; Wang, Y.; Yang, W.; Zhan, Y. *Dye. Pigment.* **2021**, *194*, 109542.
 - (31) Li, W.; Pan, Y.; Xiao, R.; Peng, Q.; Zhang, S.; Ma, D.; Li, F.; Shen, F.; Wang, Y.; Yang, B.; Ma, Y. *Adv. Funct. Mater.* **2014**, *24*, 1609.
 - (32) Li, W.; Pan, Y.; Yao, L.; Liu, H.; Zhang, S.; Wang, C.; Shen, F.; Lu, P.; Yang, B.; Ma, Y. *Adv. Opt. Mater.* **2014**, *2*, 892.
 - (33) Jiang, J.; Li, X.; Hanif, M.; Zhou, J.; Hu, D.; Su, S.; Xie, Z.; Gao, Y.; Yang, B.; Ma, Y. *J. Mater. Chem. C* **2017**, *5*, 11053.
 - (34) Loythaworn, T.; Petdee, S.; Chasing, P.; Chantanop, N.; Therdkatanyuphong, P.; Waengdongbung, W.; Sudyoasuk, T.; Promarak, V. *Mater. Chem. Front.* **2022**, *6*, 3225.
 - (35) Liu, T.; Chen, X.; Zhao, J.; Wei, W.; Mao, Z.; Wu, W.; Jiao, S.; Liu, Y.; Yang, Z.; Chi, Z. *Chem. Sci.* **2021**, *12*, 5171.
 - (36) Sudyoasuk, T.; Petdee, S.; Chasing, P.; Therdkatanyuphong, P.; Kaiyasuan, C.; Waengdongbung, W.; Namuangruk, S.; Promarak, V. *Dye. Pigment.* **2021**, *195*, 109712.
 - (37) Tagare, J.; Vaidyanathan, S. *J. Mater. Chem. C* **2018**, *6*, 10138.
 - (38) Yu, Y.; Cang, M.; Cui, W.; Xu, L.; Wang, R.; Sun, M.; Zhou, H.; Yang, W.; Xue, S. *Dye. Pigment.* **2021**, *184*, 108770.
 - (39) Kongsabay, S.; Funchien, P.; Chasing, P.; Sudyoasuk, T. *J. Lumin.* **2022**, *248*, 118921.
 - (40) Yu, Y.; Chao, X.; Xie, M.; Zhou, Y.; Ma, C.; Zhou, H. *Dye. Pigment.* **2023**, *215*, 111306.
 - (41) Jairam, T.; Hong, W. P. *J. Mater. Chem. C* **2022**, *51*, 16173.

- (42) Liu, Y.; Liu, H.; Bai, Q.; Du, C.; Shang, A.; Jiang, D.; Tang, X.; Lu, P. *ACS Appl. Mater. Interfaces* **2020**, *12*, 16715.
- (43) Liu, Y.; Man, X.; Bai, Q.; Liu, H.; Liu, P.; Fu, Y.; Hu, D.; Lu, P.; Ma, Y. *CCS Chem.* **2022**, *4*, 214.
- (44) Wang, C.; Li, X.; Pan, Y.; Zhang, S.; Yao, L.; Bai, Q.; Li, W.; Lu, P.; Yang, B.; Su, S.; Ma, Y. *ACS Appl. Mater. Interfaces* **2016**, *8*, 3041.
- (45) Sudyoardsuk, T.; Petdee, S.; Waengdongbung, W.; Loythaworn, T.; Chasing, P.; Kongsabay, S.; Therdkatanyuphong, P.; Promarak, V. *Adv. Photonics Res.* **2023**, *4*, 2200195.
- (46) Li, Y.; Yao, J.; Wang, C.; Zhou, X.; Xu, Y.; Hanif, M.; Qiu, X.; Hu, D.; Ma, D.; Ma, Y. *Dye. Pigment.* **2020**, *173*.
- (47) Chen, X.; Ma, D.; Liu, T.; Chen, Z.; Yang, Z.; Zhao, J.; Yang, Z.; Zhang, Y.; Chi, Z. *CCS Chem.* **2022**, *4*, 1284.
- (48) Xia, H.; Xu, X.; Guo, J.; Qian, C.; Zhang, K.; Zhu, M.; Zhang, B.; Peng, W.; Peng, Q.; Zhu, W. *Dye. Pigment.* **2021**, *186*, 108950.
- (49) Huang, X.; Zhang, G.; Zhou, C.; Liu, S.; Zhang, J.; Ying, L.; Huang, F.; Cao, Y. *New J. Chem.* **2015**, *39*, 3658.
- (50) Fan, J.; Zhang, Y.; Zhang, K.; Liu, J.; Jiang, G.; Li, F.; Lin, L.; Wang, C. K. *J. Mater. Chem. C* **2019**, *7*, 8874.
- (51) Funchien, P.; Chasing, P.; Sudyoardsuk, T.; Promarak, V. *Chem. Commun.* **2020**, *56*, 6305.
- (52) Kaewpuang, T.; Chaiwai, C.; Chasing, P.; Wongkaew, P.; Sudyoardsuk, T.; Namuangruk, S.; Manyum, T.; Promarak, V. *J. Photochem. Photobiol. A Chem.* **2021**, *420*, 113509.
- (53) Tu, L.; Xie, Y.; Li, Z.; Tang, B. *SmartMat* **2021**, *2*, 326.
- (54) Pan, Y.; Huang, J.; Li, W.; Gao, Y.; Wang, Z.; Yu, D.; Yang, B.; Ma, Y. *RSC Adv.* **2017**, *7*, 19576.
- (55) Grabowski, Z. R.; Rotkiewicz, K.; Rettig, W. *Chem. Rev.* **2003**, *103*, 3899.
- (56) Li, W.; Liu, D.; Shen, F.; Ma, D.; Wang, Z.; Feng, T.; Xu, Y.; Yang, B.; Ma, Y. *Adv. Funct. Mater.* **2012**, *22*, 2797.
- (57) Katagiri, C.; Yoshida, T.; White, M. S.; Yumusak, C.; Sariciftci, N. S.; Nakayama, K. I. *AIP Adv.* **2018**, *8*, 105001.
- (58) Suzuki, Y.; Adachi, S.; Suenobu, T.; Suzuki, M.; Nakayama, K. I. *Jpn. J. Appl. Phys.* **2020**, *59*, SDD01.
- (59) Gao, M.; Burn, P. L.; Pivrikas, A. *ACS Photonics* **2021**, *8*, 2425.
- (60) Gao, M.; Burn, P. L.; Pivrikas, A. *J. Appl. Phys.* **2019**, *126*, 035501.
- (61) Peng, H.; Wang, W.; Chen, S. *IEEE Electron Device Lett.* **2015**, *36*, 369.
- (62) Li, Z.; Hu, X.; Liu, G.; Tian, L.; Gao, H.; Dong, X.; Gao, T.; Cao, M.; Lee, C. S.; Wang, P.; Wang, Y. *J. Phys. Chem. C* **2021**, *125*, 1980.
- (63) Chan, L. H.; Lee, R. H.; Hsieh, C. F.; Yeh, H. C.; Chen, C. T. *J. Am. Chem. Soc.* **2002**, *124*, 6469.
- (64) Ji, W.; Jing, P.; Xu, W.; Yuan, X.; Wang, Y.; Zhao, J.; Jen, A. K. Y. *Appl. Phys. Lett.* **2013**, *103*, 053106.
- (65) Juang, F. S.; Yao, M. Q.; Mondal, T.; Saha, S. K. *IEEE Access* **2020**, *8*, 216986.
- (66) Frisch, M. J.; Trucks, G. W.; Schlegel, H. B.; Scuseria, G. E.; Robb, M. A.; Cheeseman, J. R.; Scalmani, G.; Barone, V.; Petersson, G. A.; Nakatsuji, H.; Li, X.; Caricato, M.; Marenich, A. V.; Bloino, J.; Janesko, B. G.; Gomperts, R.; Mennucci, B.; Hratchian, H. P.; Ortiz, J. V.; Izmaylov, A. F.; Sonnenberg, J. L.; Williams-Young, D.; Ding, F.; Lipparini,

F.; Egidi, F.; Goings, J.; Peng, B.; Petrone, A.; Henderson, T.; Ranasinghe, D.; Zakrzewski, V. G.; Gao, J.; Rega, N.; Zheng, G.; Liang, W.; Hada, M.; Ehara, M.; Toyota, K.; Fukuda, R.; Hasegawa, J.; Ishida, M.; Nakajima, T.; Honda, Y.; Kitao, O.; Nakai, H.; Vreven, T.; Throssell, K.; Montgomery, J. A., Jr.; Peralta, J. E.; Ogliaro, F.; Bearpark, M. J.; Heyd, J. J.; Brothers, E. N.; Kudin, K. N.; Staroverov, V. N.; Keith, T. A.; Kobayashi, R.; Normand, J.; Raghavachari, K.; Rendell, A. P.; Burant, J. C.; Iyengar, S. S.; Tomasi, J.; Cossi, M.; Millam, J. M.; Klene, M.; Adamo, C.; Cammi, R.; Ochterski, J. W.; Martin, R. L.; Morokuma, K.; Farkas, O.; Foresman, J. B.; Fox, D. J. Gaussian 16, Revision C.01; Gaussian, Inc.: Wallingford, CT, 2016.